Impact of the meso-texture on the exctinction behaviour of architected porous ceramics: from spatial correlation characterizations up to (non) beerian radiative behaviour evaluation

Benoit Rousseau, Y. Favennec, Jérôme Vicente, Franck Enguehard

IMPACT OF THE MESO-TEXTURE ON THE EXCTINCTION BEHAVIOUR OF ARCHITECTED POROUS CERAMICS: FROM SPATIAL CORRELATION CHARACTERIZATIONS UP TO (NON) BEERIAN RADIATIVE BEHAVIOUR EVALUATION

B. Rousseau[1], Y. Favennec[1], J. Vicente[2], F. Enguehard[3]

[1]Nantes Université, CNRS, LTeN, Nantes, 44306, France
[2]Aix Marseille University, CNRS, IUSTI, Marseille, 13453, France
[3]Université de Poitiers, ISAE-ENSMA, CNRS, Institut P', Futuroscope Chasseneuil, 86360, France

ABSTRACT

So far the firm link between the spatial arrangement of consolidated porous ceramics and their ability to attenuate the thermal radiation along its direction of propagation remains a topic of debate. This is particularly true for architected ceramics with regular topologies, obtained by additive manufacturing. To cope with this issue, numerical 3D geometries with different arrangement of cells (regular and irregular) will be generated with genMat an homemade software. Then, the two-point correlation functions of each architecture will be computed to precise the type of spatial correlations prevailing in the medium. The analysis of the extinction cumulative distribution function curves obtained with the Radiative Distribution Function Identification method allows us to check whether or not if the attenuated thermal radiation follows an exponential decay as it the case for Beerian media. Effect of the cell size, cell numbers and cell geometries will be discussed. Finally, preliminar practical considerations will be given for making the distinction between Beerian and non Beerian 3D architectures.

KEY WORDS: Architected refractory ceramics, correlated media, Radiative Distribution Function Identification, non beerian behaviour.

1. INTRODUCTION

In the field of carbon-free heat generation and waste heat recovery at high temperatures (T>1000°C), there is a growing interest in the design of compact and long-life high temperature energy systems (HTES) such as gas-to-gas heat exchangers [1], volumetric solar receivers [2] (VSR) and radiant tube inserts [3], among others. These HTES can be described as radiative convective heat exchangers [4]. Advanced HTES, intensively studied today at lab scale, are mostly based on architected refractory ceramics (p ~75-95%, cell size ~0.5-10 mm) which can be depicted by a continuous ligament network (the solid phase) delimiting open or closed cells, periodically or pseudo-randomly arranged in space [5]. The whole 3D architecture exhibits therefore outstanding properties such as high strength-to-weight ratio, high specific surface area, good flow-mixing capacity. According to the intrinsic chemical and physical properties of the material used in the elaboration of the solid phase, the 3D architectures can display additionally high thermal shock resistance, good effective thermal conductivity, high thermal emissivity and high resistance to chemical corrosion. These latter properties can be reached in particular when silicon carbide (SiC)-based compounds are considered [2, 6]. The rapid development of additive manufacturing (AM) opens today the gates to elaborate a large range of 3D geometries going from regular lattice structures with different types of unit cells (cube, honeycomb, Kelvin, Weaire-Phelan, octet, star, among others), triply periodic minimal surface-based structures (D-surface, gyroid, neovius, among others) up to more classical irregular strut-based structures (open-cell foams, voronoi lattices). Multi-lattice structures can be also designed by combining several stacks constituted of a given type of cell [7]. Such multi-lattice structures can also exhibit a gradual cell size configuration [5, 7] either axially, along the main axis of heat transfer, or radially [3]. In order to propose a topology optimization process aiming at the definition of the best 3D architectures for a prescribed thermal objective, the fine

*Corresponding Author : benoit.rousseau@univ-nantes.fr

modelling of their thermal behaviour is here essential [3, 8]. In particular, one of the main challenges, is to be able to exactly describe the role of thermal and/or solar radiation in the heat balance of the system for both unsteady or steady regimes. To date, two main routes can be used to determine the temperature and/or heat flux fields within 3D structures [8-11]. The first class of methods, at the discrete mesoscopic scale, allows a treatment of the radiative heat exchange directly at the scale of the individual constituents (here the struts and walls constituting the basic cells). The discrete scale method gives results that are more accurate but at the price of high computational costs especially when the volume of the numerical domain imposed by the 3D architecture is higher or close to the representative elementary volume. Several parallelized approaches have been developed for that purpose : stabilized vectorial Finite Element schemes [8], cell centered Finite Volume models associated to ray tracing [12, 13], hybrid scheme combining motion of Brownian walkers in the solid opaque phase and ray tracing in the fluid phase [14], and Monte Carlo strategy based on integral formulation [15]. The second class of method, at the continuous macroscopic scale, requires to rigorously solve the radiative transfer equation as long as the assumptions (randomness, homogeneity and continuity) that govern its statement are valid. Let us precise that an architected ceramic can be viewed as an equivalent domain absorbing, emitting and scattering the thermal radiation, these phenomena being induced by light-matter interaction at the scale of the ligaments. If the equivalent medium is optically thick, the radiative transfer equation can be reduced to a more simple diffusion equation by applying for example the spherical harmonics method at the order 1 (P1 approximation) and, even more crudely, the Rosseland approximation [9]. Whatever the precision sought, these approaches can be only applied if the volume radiative properties (extinction, absorption and scattering coefficients, scattering phase function) are identified from an equivalent semitransparent continuous Beerian medium. The term Beerian stands, here, for an extinction law characterised by an exponential function of the optical thickness. From a radiative viewpoint, the medium must be, in principle, constituted of individual objects (particles, grains, fibers) spatially uncorrelated. This statement changes when spatial correlations occur meaning that the equivalent semitransparent medium becomes not easily homogeneisable. In this case, the extinction coefficient conventionally obtained by adding the individual contribution of the scatterers must be successively corrected by a scaling factor computed from the radial distribution function which depicts, here, the spatial correlations [16]. This leads to the appearance of either super-exponential or sub-exponential extinction coefficients respectively for negative and positive correlated medium [17]. When the solid matter is connected, as it the case for architected ceramics, few studies have established a firm link between the spatial organisation of the scatterers and their radiative properties. In general, the samples are considered as Beerian media [3, 7, 18] without a detailed investigation of their ability to transport radiation having been carried out beforehand. By using the radiative distribution function identification method, Taine et al. have shown that a dispersion of overlapping transparent spheres in an opaque continuous hosting medium deviates from the Beerian behavior when its volume fraction, f_v, becomes important ($f_v > 0.4$) [19]. Such a synthetic medium can be used to represent a statistically isotropic foam. Guevelou et al. computed the extinction cumulative distribution functions of virtual SiC-based irregular samples (cubic open-cell foams with domain size, L = 4.8-mm) for variable nominal pore diameters ($d_{nom} \in$ [0.25-1.1 mm]) and fixed porosity (p=0.7) and concluded that they complied with a Beerian behavior [20]. More recently, Ouchtout et al. have computed the temperatures fields within a SiC-based regular cubic lattice (p = 0.9, d_{nom}= 0.15 mm, L = 0.3 and 0.65 mm) by solving a conductive-radiative numerical scheme with stabilized vectorial finite element methodologies applied respectively at both the continuous scale and the discrete scale. Both the temperature profiles are closely identical [8]. Since the continuous approach assumes for the radiative part that the Beer law is valid, it can be concluded that this cubic lattice exhibits a Beerian behavior. Such a survey indicates that a study investigating the radiative behavior of synthetic lattices as a function of variable textural features (spatial repartition, shape and size of cells, size of the computing domain) is still relevant. To go one step further with these issues, a set of virtual regular and irregular SiC-based structures (cubic cell structures, Kelvin cell structures, gyroids, and open-cell foams) with prescribed textural features ($d_{nom} \in$ [0.5-10 mm], $L \in$ [10 -100 mm], $p \sim 0.92$, regular and irregular) will be designed with the genMat software (C++, Qt) [21]. Their two-point auto-correlation functions for the void phase will be systematically computed.

Then, the radiative distribution function identification method will be applied to compute the extinction cumulative distribution functions of the whole set of numerical samples. This will allow us to provide preliminar practical criteria for defining the radiative behaviors (non Beerian or Beerian) of the samples.

2. NUMERICAL METHODOLOGIES

2.1 3D structures generation

In this work, a homemade 3D structures generator, called genMat (C++, Qt) [21], has been used to provide the whole set of numerical samples. The generator allows the numerical elaboration of regular and irregular 3D structures with prescribed textural features (porosity, nominal pore diameter). It was initially settled for designing open-cell foams with realistic textural features [20]. For irregular open cell foams, four main steps must be followed. Firstly, the cell centers are positioned at the apexes of a regular tetrahedral network. A random perturbation, whom the value is lower than the side tetrahedron, is performed for slightly displacing the centers. Secondly, a fast marching-cube process is implemented with the aim to reproduce a realistic bubbling process. A distance map, where each voxel knows the value of the space separating it from the nearest neighboring center, is created. This set-up permits the simultaneous growth of the entire cells and avoids eventual overlaying. A watershed algorithm is afterwards applied on the distance map for the segmentation of the void phase and the solid phase by a Voronoï tessellation process. As such, a thin continuous skeleton of the 3D structures can be obtained. Thirdly, each strut is shaped with a spherical structuring element of variable side. Finally, in order to accurately tune the final porosity, the fast-marching algorithm is again used to compute a distance map within the void phase from the solid–void interface. The resulting distance map is then converted into grey level for which the adequate binarization threshold provide the targeted porosity. For the regular structures, a simplified four-steps process can be followed where centers of all cells are firstly created. Secondly, the nodes, edges, faces of all cells are defined, and a structuration loop adds solid voxels between each apex, forming a thin skeleton. Thirdly, as for irregular foams, the ligaments can be shaped with a spherical structuring element. Lastly, the desired porosity is reached by creating, as for the irregular foams, a distance map converted in grey levels. Once the 3D binarized structures are generated, a robust marching cube process allows to mesh the fluid/solid interface. GenMat proposes an export module for recording surfacic meshes. Let us precise that for triply periodic minimal surface-based structures, a Matlab script is used to produce the 3D meshed geometries, which are afterwards imported in genMat.

2.2 Textural properties characterization

genMat contains also modules which provide the volume fraction of the void phase i.e. the porosity, p, and the volumetric surface, A of each numerical sample. For this work, a supplementary routine has been added for computing their two-point correlation functions by following the process described in the reference book of Torquato [22]. Briefly, by using a given binarized 3D image, its phase or indicator function, $Z^f(\boldsymbol{x})$ of the void or fluid space can be determined. Here $\boldsymbol{x}$ is the position vector. $Z^f(\boldsymbol{x})$ is equal to 1 if $\boldsymbol{x}$ belongs to the void phase and, otherwise, to 0. The two-point correlation function, $S_2^f(\boldsymbol{x_1}, \boldsymbol{x_2})$, is defined by:

$$S_2^f(\boldsymbol{x_1}, \boldsymbol{x_2}) = \langle Z^f(\boldsymbol{x_1}) Z^f(\boldsymbol{x_2}) \rangle \quad (1)$$

The angular brackets represent the statiscal average. This second-order descriptor can be interpreted as the probability that two randomly points $\boldsymbol{x_1}$ and $\boldsymbol{x_2}$ both belong to the fluid phase. If the medium is statically homogenous and isotropic, S_2^f depend only on the segment of length $r = |\boldsymbol{r}|$, such as :

$$S_2^f(\boldsymbol{x_1}, \boldsymbol{x_2}) = S_2^f(|\boldsymbol{r}|) \tag{2}$$

where the displacement vector $\boldsymbol{r} = \boldsymbol{x_2} - \boldsymbol{x_1}$. Generally, for $\boldsymbol{r}$ = 0, $S_2^f(0) = p$ and in the absence of any long-range order,

$$\lim_{|\boldsymbol{r}|\to\infty} S_2^f(|\boldsymbol{r}|) \to p^2 \tag{3}$$

The analysis of the shape of $S_2^f(|\boldsymbol{r}|)$ provides useful information on how a natural or synthetic porous medium is structured [22]. In the case of artificial media, many studies taking into account $S_2^f(|\boldsymbol{r}|)$ have focused on packed beds. Thus, for a non-penetrable monodisperse sphere model of packed bed, $S_2^f(|\boldsymbol{r}|)$ decreases quasi lineraly at short $|\boldsymbol{r}|$ and then exhibit an oscillary behavior up to the asymptotic value p^2. The distance after which $S_2^f(|\boldsymbol{r}|)$ becomes asymptotic is the correlation length. On the contrary, when spheres can overlap, after the linearly decrease previously evoked, the oscillations disapear. Let us underline that for a perfect regular arrangement of spheres, the amplitudes and the periods of the oscillations remain identical for growing values of $|\boldsymbol{r}|$. $S_2^f(|\boldsymbol{r}|)$ can be mathematicaly described from an exponentially decaying function and more sophiticated expresions are available to reproduce damped oscillation. This brief overwiew can be used to analysis the textural behavior of any porous media.

2.3 Radiative distribution function identification method

In this work, the radiative distribution function identification (RDFI) method, originally proposed by Tancrez and Taine [23], will be applied to determine the volumetric radiative properties of the 3D architectures numerically generated. This method had been implemented in the genMat framework [20]. More precisely, the RDFI is a collision-based Monte Carlo Ray Tracing method assuming that for each local interaction between a ray and the solid matter, the geometrical optic approximation is valid. It means that the mean characteristic size of the ligaments and of the cells constituting the generated 3D structures must be much larger than the incident wavelength i.e. the Mie size parameter is greater than 1. The RDFI method consists in launching a huge number of rays from M points that are uniformly distributed in the fluid phase surrounding the ligaments. Their directions are randomly chosen within the entire 4π steradian sphere. Once a ray hits a solid phase element at the point I, it is considered as totally extinguished and the path length to collision, $s_e = |MI|$ is computed. For a large number of rays, N_R, a set of path length $s_{e,j}$ values are obtained from which the corresponding normalized extinction distribution function, $F_e(s)$ is computed :

$$F_e(s) = \frac{1}{N_r}\sum_{j=1}^{N_R} \delta\left(s - s_{e,j}\right) \tag{4}$$

where s is the path length variable and δ the Dirac delta distribution. The extinction cumulative distribution function $G_e(s)$ is then obtained by integrating $F_e(s)$:

$$G_e(s) = \int_0^s F_e(s')s' \tag{5}$$

To decide whether the extinguished ray is absorbed or scattered, a random number, η, uniformly distributed over [0,1] is selected and compared to the local reflectivity, ρ, that can be given by the Fresnel law (if the interacting fluid/solid interface is considered as optically smooth). If $\eta > \rho$ the ray is considered as absorbed and otherwise scattered. This allows to determine the absorption and the scattering cumulative probability with a similar numerical process than for $G_e(s)$. If the studied

equivalent medium is Beerian, the quantity $\left(1 - G_e(s)\right)$ shows a typical Beer-Lambert exponential decay behaviour expressed by:

$$1 - G_e(s) = e^{-\beta s} = \frac{I(s)}{I_0} \tag{6}$$

where $I(s)$ is the radiant intensity at the distance s and I_0 is the impinging intensity at s = 0 from a collimated beam. In that situation, the extinction coefficient β of the equivalent medium can be evaluated by a fit of the numerically evaluated $\left(1 - G_e(s)\right)$ function.

3. RESULTS AND DISCUSSION

In the following, the room-temperature complex refractive index of silicon carbide at the wavelength of 4 µm, is affected to the solid skeleton of each numerical 3D structure [21]. It ensures that their ligaments can be considered as optically thick, their lowest diameter being fixed at 400 µm. The computational domains have a cubic geometry with a side, L, of 50 mm. For a sake a clarity, the acronyms CCS, KCS, GS and OCFS represent respectively cubic cell structures, Kelvin cell structures, gyroid structures and open-cell foam structures. To complete their denomination, one adds an information for the d_{nom}, the number of cell, N_c, and the size of the domain. CCS_10_125_50 depicts a cubic cell structures with d_{nom} = 10 mm, N_c= 125 and L = 50 mm.

3.1 Influence of the spatial correlations for regular and irregular structures

Four 3D structures (L = 50 mm, d_{nom}~ 10 mm, voxel number = 500^3, voxel size = 100 µm) are generated with genMat.

Table 1 Textural and radiative parameters

Samples	p	A (m^{-1})	β^{om}(m^{-1})	a	b (m^{-1})
CCS_10_125_50	0.93	138.2	36.9	1.20	43.1
KFS_10_125_50	0.93	256.7	68.7	2.79	28.7
GS_10_125_50	0.95	330.0	86.7	3.76	28.4
OCFS_10_125_50	0.93	297.2	79.9	6.55	20.0

Table 1 gives their respective porosity and volumetric surface after having performed the final porosity tuning process as explained in section 2.1. Fig.1 depicts the synthetic 3D images where open channels can be obviously observed for CCS_10_125_50 and KCS_10_125_50. The two-point correlations, computed for all the directions, are plotted in Fig. 2a). For CCS_10_125_50, KCS_10_125_50 and GS_10_125_50, the curves show similar features namely a rapid quite linear decay at short r followed by several oscillations, at larger r, with the periodicity imposed by the spatial arrangement of their respective unit cells. This is reflective of spatial correlations between the constituents of the structures [22]. Note that for KCS_10_125_50 and GS_10_125_50, the amplitude of the oscillations are less intense than for CCS_10_125_50, meaning that the effect of the spatial periodicity for the range of r investigated is less pronounced. It can be noticed also that the slopes of the linear decay, as expected, is all the more sharp than A is important (see Table 1). For OCF_10_125_50, the shape of $S_2^f(|\boldsymbol{r}|)$ is rather different with a first sharp decay at the shorts r followed by a slower decreasing at higher r. Slight oscillations can be seen. This indicates that the ligaments of OFC_10_125_50 appears as being less correlated than the others structures.

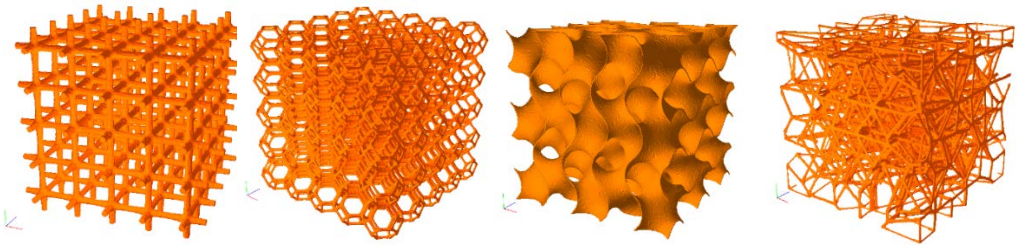

Fig.1 3D images of 4 porous structures with L = 50 mm, p ~0.93 and d_{nom}~10 mm (1) CCS_10_125_50 (2) KCS_10_125_50, (3) GS_10_125_50 (4) OCFS_10_125_50

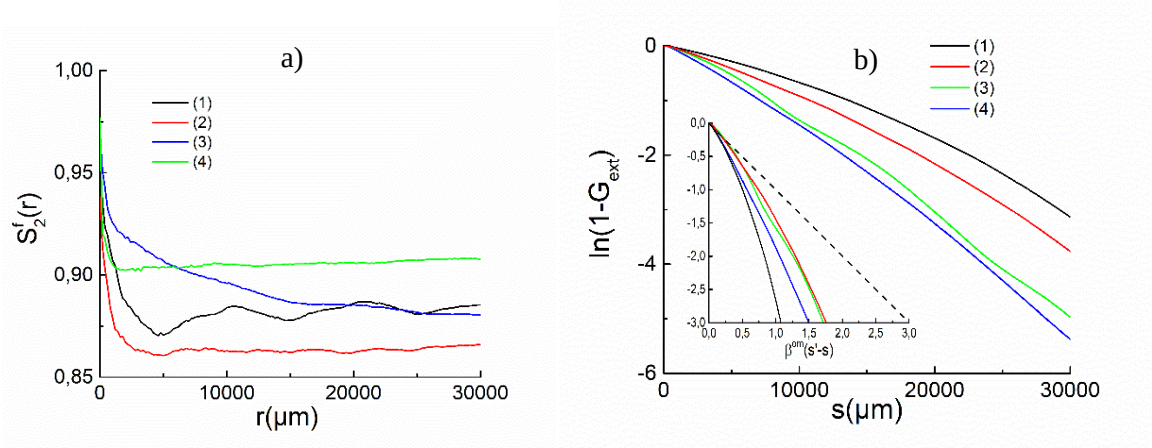

Fig.2 a) Two-point autocorrelation function: (1) CCS_10_125_50, (2) KCS_10_125_50, (3) GS_10_125_50 (4) OCFS_10_125_50, b) Extinction cumulative distribution function: (1) CCS_10_125_50, (2) KCS_10_125_50, (3) GS_10_125_50 (4) OCFS_10_125_50.

Fig. 2b) shows extinction cumulative distribution functions $ln\left(1 - G_e(s)\right)$ as a function of s, obtained for N_R = 10^6. Such a value of N_R guarantees to results statistical flutuations less than 0.1. Special care has been taken to define a suitable shooting zone for computing $ln\left(1 - G_e(s)\right)$ i.e., not too small to be representative, and not too large to limit outgoing rays. Only a central zone of 400^3 voxels is considered for each computation. Two behaviours can be observed in Fig. 2b). CCS_10_125_50 and KCS_10_125_50 present curves which deviate clearly from what is expected for a Beerian behaviour, whereas GS and OCFS exhibit a more linear feature. In the insight part of Fig.2b) the same curves are given in function of the optical thickness $\beta^{om}(s' - s)$, β^{om} being the value of the extinction of the optically thin limit ($\beta^{om} = A/4p$). They display a similar radiative behaviour than those described by Shaw et al. for negatively correlated particulate media [17]. It is worth of notify that the extinction cumulative distribution function curve of OCFS_10_125_50 shows the more linear feature knowing that this 3D structure is surely the less spatially correlated. In the opposite, CCS_10_125_50 have the stronger non-Beerian feature whereas it is the more spatially correlated. Higher values of β^{om} that can be numerically settled, for similar values of p and L by an higher value of A, is likely to confer a Beerian behaviour to the 3D structures. In other words, it turns to decrease d_{nom} once p and L are imposed. To go one step further, each extinction cumulative distribution function curve has been nicely fitted thanks to a Levengberg-Marquardt scheme by the following expression:

$$y(s) = -a\left(e^{bs} - 1\right) \tag{7}$$

In Gomez-Garcia et al, the authors proposed a quite similar expression for analysing the radiation propagation within a stack of SiC-based square grids [24]. Table 1 lists values of a and b for CCS_10_125_50, KCS_10_125_50, GS_10_125_50 and OFCS_10_125_50. Going from CCS_10_125_50 up to OFCS_10_125_50, it can be evidenced from the Table 1 that the highest value

of a and the lowest value of b are required to confer a Beerian behaviour for the numerical 3D architectures. Let us now introduce a criterion accuracy ε with $b = \varepsilon/L$ and L = 50 mm. As an example, for ε = 0.1, one obtains b = 2 m^{-1} that yields $y(s) \sim 2as$ for $0 < s < L$ when the exponential term is approximated by its Taylor expansion. In this case, $\beta \sim 2a$ knowing that a is obtained through the latter fitting curve process. It suggests that obtaining values a close to threshold value of 2 m^{-1} must be concomitant with a Beerian behaviour. To highlight this quantitative criterion, two numerical samples (KFCS, OFCS) with d_{nom} = 5 mm and L = 50 mm are generated and the fits, by using Eq. 7, of their linear extinction cumulative distribution functions give respectively b = 7.3 m^{-1} and 6.8 m^{-1} (in comparison for d_{nom} = 10 mm, b = 28.7 m^{-1} and 20 m^{-1} at is reported in Table 1). By taking a cruder criterion (ε = 0.4, giving b = 8 m^{-1}), one can consider, in the following, that all extinction cumulative distribution functions for which the fitting curve process with Eq. 7 conduct to b < 8 m^{-1} should exhibit therefore a Beerian behaviour.

3.2 Influence of the cell number for a regular structure

From the previous section, it can be argued that the conjunction of weak spatial correlations and low cell size allows to confer to a 3D structure a Beerian behaviour. Let us now consider the effect of a growing number of cells with d_{nom} equals here to 5 mm. Table 2 lists the main textural parameters used to design the numerical samples by genMat with 2^3, 4^3, 6^3, 8^3 and 10^3 cells. The numerical samples are described in Fig.3

Table 2 Textural and radiative parameters

Samples	p	L (mm)	A (m^{-1})	β^{om}(m^{-1})	a	b (m^{-1})
CCS_5_8_15	0.94	15	232.1	61.73	0.71	204.46
CCS_5_64_25	0.93	25	252.6	67.90	1.65	76.10
CCS_5_216_35	0.93	35	268.2	72.10	2.78	41.96
CCS_5_512_45	0.93	45	278.1	74.76	5.07	23.45
CCS_5_1000_55	0.93	55	283.7	76.26	6.23	16.99

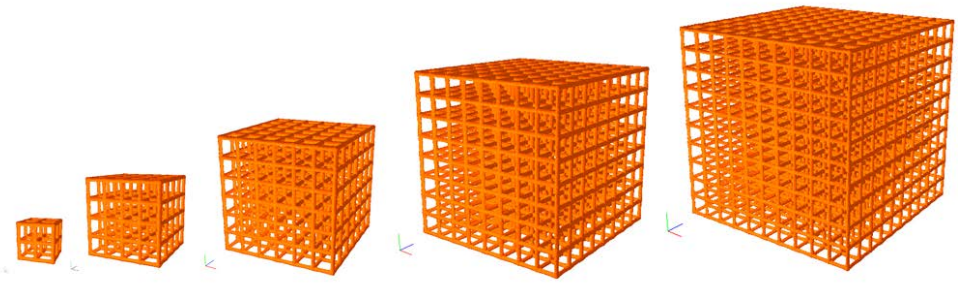

Fig.3 3D images of (1) CCS_5_8_15 (2) CCS_5_64_25, (3) CCS_5_216_35, (4) CCS_5_512_45, (5) CCS_5_1000_55

Their two-point autocorrelation functions are given as a function of r/L in Fig. 4a). The amplitudes of the oscillations tend to decrease as L becomes large. It means the influence of the lattice periodicity weakens when the size of the computational domain is important. Moreover, the slopes of the curves increase when N_c grows up that is coherent with the computation of A with genMat. Corollary, as it is reported in Fig4b), the structures present a non Beerian feature less and less pronounced when N_c comes to be large. A similar trend can be found for numerical samples of the KFS family (except for N_c = 8) with same characteristic size. The non Beerian feature turns to be less important when the spatial correlations imposed by the 3D architecture vanish at large r. By performing a fit process, based on Eq. (7), the curves of Fig4b) are perfectly reproduced. For each curves the residuals are less than 0.05. As given in Table 2, it can be notified that for an increasing value of N_c, a grow up and b decline, the

product ab becoming more important. But according to the criterion proposed in the last section, it would be necessary to have larger L (> 50 mm) to tend towards the Beerian case.

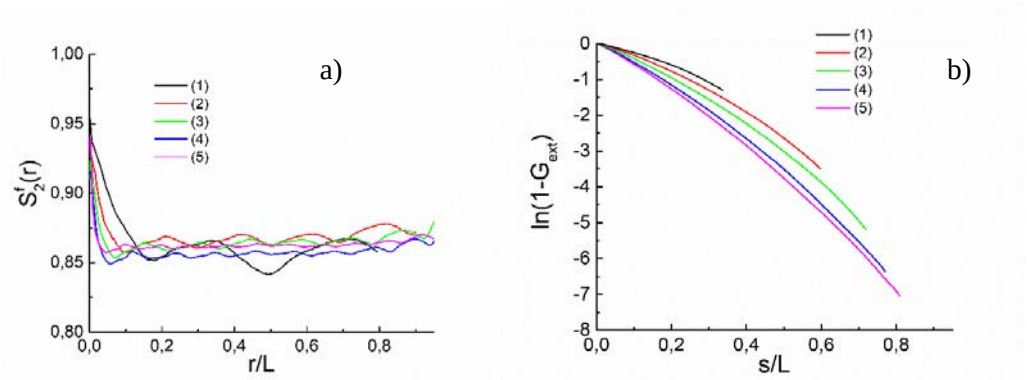

Fig4 a) Two-point autocorrelation function: (1) CCS_5_8_10, (2) CCS_5_64_20, (3) CCS_5_216_30, (4) CCS_5_512_40, (5) CCS_5_1000_50 b) Extinction cumulative distribution function: (1) CCS_5_8_10, (2) CCS_5_64_20, (3) CCS_5_216_30, (4) CCS_5_512_40, (5) CCS_5_1000_50

3.3 Influence of the domain size for regular structures with same number of cells

Let us now investigate the effect of the size of the computational domain for Kelvin-cell structures with a same number of cells (N_c = 1000) but with a decreasing domain size (L is going from 50 up to 5 mm). N_c = 1000 ensures that the medium presents the best Beerian feature. This means that d_{nom} falls down from 5 to 0.5 mm. In parallel, A grows up softly when L decreases from 50 to 30 mm to reach then more abruptly very high values when L drops at 5 mm (see Table 3).

Table 3 Textural and radiative parameters

Samples	p	L (mm)	A (m^{-1})	β^{om}(m^{-1})	a	b (m^{-1})
KFS_0.5_1000_5	0.91	5	5049	1387.10	8.39	176.9
KFS_1_1000_10	0.91	10	2888	793.10	13.6	65.5
KFS_2 _1000_20	0.91	20	1309	359.62	10.1	39.2
KFS_3 _1000_30	0.91	30	1007	273.64	22.7	13.6
KFS_4 _1000_40	0.91	40	690	185.48	18.6	11.7
KFS_5_1000_50	0.91	50	546	148.37	17.2	9.9

In Fig.5a), the two-point autocorrelation functions for the fluid phase of the whole set of samples can be nicely superimposed when they are given as a function of r/L. The homothetic process tends to preserve the spatial correlations prevailing in KFS_5_1000_50. The extinction cumulative distribution function curves depicted in Fig. 5b) appears to be quite similar that is consistent with the preservation of the spatial arrangement of the network during the homothetic process. The curve fitting process reveals that the product ab drops with the same rate than β^{om}. However, whereas b decreases from L = 5 mm up to L = 50 mm, a shows an inhomogeneous evolution. A similar homothetic scheme applied to a set of 125 Kelvin cells forming a cubic domain with decreasing L (from 50 mm down to 5 mm) confirms the latter evolution namely the extinction behaviour is preserved. In this case, the extinction cumulative distribution function curves can be fitted with Eq. 7 given b = 34.2 m^{-1} that is typical of a non-Beerian feature. From Table 3, it appears that KFS_5_1000_50 is the sample that can show the best Beerian. In doing so, its extinction coefficient will be 8a namely 137.6 m^{-1}. Let us recall that only for such a case, the application of a continuous scale method, based on the Beerian framework, for solving the radiative transfer equation is required for any heat transfers issues.

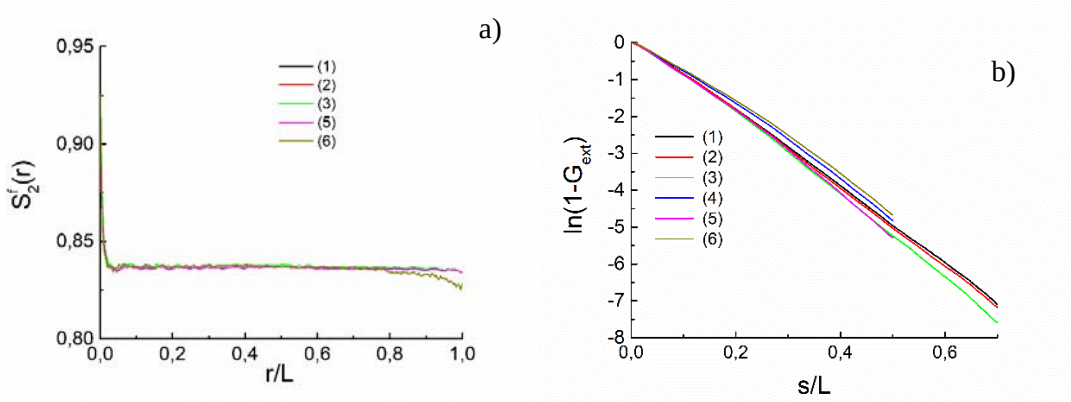

Fig 5 a) Two-point autocorrelation function: (1) KFS_5_1000_50, (2) KFS_4_1000_40, (3) KFS_3_1000_30, (4) KFS_2_1000_20, (5) KFS_1_1000_10, (6) KFS_0.5_1000_5 b) Extinction cumulative distribution function: (1) KFS_5_1000_50, (2) KFS_4_1000_40, (3) KFS_3_1000_30, (4) KFS_2_1000_20, (5) KFS_1_1000_10, (6) KFS_0.5_1000_5

4 CONCLUSION

This work combines the numerical generation of highly porous 3D architectures (CCS, KFS, GS and OFCS) with a continuous solid networks and the determination of their respective two-point correlation functions and extinction cumulative distribution functions. All the numerical samples are spatially correlated with a degree of correlations which reduces when the structures become irregular. In turn, weak spatial correlations favour a Beerian behaviour which are all so more important that the volumetric surface is important. For non Beerian 3D structures, which are mainly periodic architected structures, a practical exponential growth law is given to describe their extinction behaviour as a function of the variable path length. A preliminary criterion is provided to make a discrimination between Beerian and non Beerian architectures from the fitting curve process of their extinction cumulative distribution functions. For this class of architected materials, more works are now required to establish a firm link between their extinction behaviours and their first- and second-order textural features.

ACKNOWLEGDEMENT

The authors thank the French Research Network called GDR TAMARYS and funded by CNRS for providing motivating and high-level framework for scientific exchanges.

NOMENCLATURE

A	volumetric surface	[m^{-1}]	f_v	volume fraction	
F_e	normalized extinction distribution function		p	porosity	
G_e	extinction cumulative function distribution		$\boldsymbol{r}$	displacement vector	
I	radiant intensity		s	path length variable	[µm]
L	domain size	[mm]	s_e	path length to collision	[µm]
N_c	number of cells		$\boldsymbol{x_i}$	vector position at the point i	
S_2^f	two-point correlation function		β	extinction coefficient	[m^{-1}]
Z^f	indicator function for the fluid phase		β^{om}	β at the optically thin limit	[m^{-1}]
d_{nom}	nominal pore diameter	[µm]			

REFERENCES

[1] Bayaniahangar R, Okoh I, Nawaz K, Cesarano J, Bigham S. Toward extreme high-temperature supercritical CO2 power cycles: Leakage characterization of ceramic 3D-printed heat exchangers. Additive Manufacturing. 2022;54:102783.
[2] Heisel C, Caliot C, Chartier T, Chupin S, David P, Rochais D. Digital design and 3D printing of innovative SiC architectures for high temperature volumetric solar receivers. Solar Energy Materials and Solar Cells. 2021;232:111336.
[3] Pelanconi M, Barbato M, Zavattoni S, Vignoles G, Ortona A. Thermal design, optimization and additive manufacturing of ceramic regular structures to maximize the radiative heat transfer. Materials & Design. 2019;163:107539.
[4] Luque S, Menéndez G, Roccabruna M, González-Aguilar J, Crema L, Romero M. Exploiting volumetric effects in novel additively manufactured open solar receivers. Solar Energy. 2018;174:342-51.
[5] Pelanconi M, Rezaei E, Ortona A. Cellular ceramic architectures produced by hybrid additive manufacturing: A review on the evolution of their design. Journal of the Ceramic Society of Japan. 2020;128:595-604.
[6] Pelanconi M, Zavattoni S, Cornolti L, Puragliesi R, Arrivabeni E, Ferrari L, et al. Application of ceramic lattice structures to design compact, high temperature heat exchangers: material and architecture selection. Materials. 2021;14:3225.
[7] Avila-Marin AL, Fernandez-Reche J, Gianella S, Ferrari L, Sanchez-Señoran D. Experimental study of innovative periodic cellular structures as air volumetric absorbers. Renewable Energy. 2022;184:391-404.
[8] Ouchtout S, Rousseau B, Favennec Y. Finite element framework for modeling conducto-radiative transfers within heterogeneous media at both discrete and continuous scales. International Journal of Heat and Mass Transfer. 2022;197:123274.
[9] Avila-Marin A, Fernandez-Reche J, Martinez-Tarifa A. Modelling strategies for porous structures as solar receivers in central receiver systems: A review. Renewable and Sustainable Energy Reviews. 2019;111:15-33.
[10] Petrasch J, Haussener S, Lipiński W. Discrete vs. continuum-scale simulation of radiative transfer in semitransparent two-phase media. Journal of Quantitative Spectroscopy and Radiative Transfer. 2011;112:1450-9.
[11] Xia X-L, Li Y, Sun C, Ai Q, Tan H-P. Integrated simulation of continuous-scale and discrete-scale radiative transfer in metal foams. Journal of Quantitative Spectroscopy and Radiative Transfer. 2018;212:128-38.
[12] Kumar A, Vicente J, Daurelle J-V, Favennec Y, Rousseau B. A numerical method based on domain decomposition to solve coupled conduction-radiation physics using parallel computing within large porous media. Journal of Physics: Conference Series: IOP Publishing; 2021. p. 012057.
[13] Perraudin DY, Haussener S. Numerical quantification of coupling effects for radiation-conduction heat transfer in participating macroporous media: Investigation of a model geometry. International Journal of Heat and Mass Transfer. 2017;112:387-400.
[14] Vignoles GL. A hybrid random walk method for the simulation of coupled conduction and linearized radiation transfer at local scale in porous media with opaque solid phases. International Journal of Heat and Mass Transfer. 2016;93:707-19.
[15] Caliot C, Blanco S, Coustet C, El-Hafi M, Eymet V, Forest V, et al. Combined conductive-radiative heat transfer analysis in complex geometry using the Monte Carlo method. 2019.
[16] Drolen B, Tien C. Independent and dependent scattering in packed-sphere systems. Journal of Thermophysics and Heat Transfer. 1987;1:63-8.
[17] Shaw RA, Kostinski AB, Lanterman DD. Super-exponential extinction of radiation in a negatively correlated random medium. Journal of quantitative spectroscopy and radiative transfer. 2002;75:13-20.
[18] Tseng CC, Swanson AD, Viskanta R, Sikorski RL, Chen MY. Effect of foam properties on radiative properties of open-cell silicon carbide foams. Journal of Quantitative Spectroscopy and Radiative Transfer. 2012;113:1503-7.
[19] Taine J, Bellet F, Leroy V, Iacona E. Generalized radiative transfer equation for porous medium upscaling: Application to the radiative Fourier law. International Journal of Heat and Mass Transfer. 2010;53:4071-81.
[20] Guevelou S, Rousseau B, Domingues G, Vicente J, Caliot C, Flamant G. Evolution of the homogenized volumetric radiative properties of a family of α-SiC foams with growing nominal pore diameter. Journal of Porous Media. 2015;18.
[21] Guévelou S, Rousseau B, Domingues G, Vicente J, Caliot C. Representative elementary volumes required to characterize the normal spectral emittance of silicon carbide foams used as volumetric solar absorbers. International Journal of Heat and Mass Transfer. 2016;93:118-29.
[22] Torquato S. Random Heterogeneous Materials Microstructure and Macroscopic Properties. 1st ed. 2002. ed. New York, NY: Springer New York; 2002.
[23] Tancrez M, Taine J. Direct identification of absorption and scattering coefficients and phase function of a porous medium by a Monte Carlo technique. International Journal of Heat and Mass Transfer. 2004;47:373-83.
[24] Gomez-Garcia F, Gonzalez-Aguilar J, Tamayo-Pacheco S, Olalde G, Romero M. Numerical analysis of radiation propagation in a multi-layer volumetric solar absorber composed of a stack of square grids. Solar Energy. 2015;121:94-102.